

On particle acceleration and trapping by Poynting flux dominated flows

Gunnar Paesold[†], Eric G. Blackman^{†‡} and Peter Messmer[¶]

[†] Department of Physics & Astronomy, University of Rochester, Rochester, NY 14627, USA

[‡] Laboratory for Laser Energetics, University of Rochester, Rochester, NY 14627, USA

[¶] Tech-X Corporation, 5621 Arapahoe Avenue, Boulder, CO 80303, USA

E-mail: paesold@pas.rochester.edu, blackman@pas.rochester.edu

Abstract. Using particle-in-cell (PIC) simulations, we study the evolution of a strongly magnetized plasma slab propagating into a finite density ambient medium. Like previous work, we find that the slab breaks into discrete magnetic pulses. The subsequent evolution is consistent with diamagnetic relativistic pulse acceleration of [10]. Unlike previous work, we use the actual electron to proton mass ratio and focus on understanding trapping vs. transmission of the ambient plasma by the pulses and on the particle acceleration spectra. We find that the accelerated electron distribution internal to the slab develops a double-power law. We predict that emission from reflected/trapped external electrons will peak after that of the internal electrons. We also find that the thin discrete pulses trap ambient electrons but allow protons to pass through, resulting in less drag on the pulse than in the case of trapping of both species. Poynting flux dominated scenarios have been proposed as the driver of relativistic outflows and particle acceleration in the most powerful astrophysical jets.

(IN PRESS, PLASMA PHYSICS AND CONTROLLED FUSION)

1. Introduction

Relativistic plasma outflows occur in the most powerful sources in the universe. The inferred Lorentz factors vary from $\sim 10^1$ in active galactic nuclei (AGN) to $> 10^2$ in gamma-ray bursts (GRB).

In AGN, it is widely believed that magnetic fields play a key role in launching and driving the observed jets, but how far away from the source (e.g. a few engine radii vs. parsec scales) the flows remain Poynting flux dominated is unresolved. A related debate for GRB is whether the relativistic outflows are powered by hot matter dominated outflows (MDO) or cold Poynting flux dominated outflows (PFDOs). In the latter, the energy is carried electromagnetically to great distances where it is finally converted to particle energy. For GRB, MDO's are constrained by the fact that too much baryon loading prevents the flow from reaching the large Lorentz factors needed to overcome the compactness problem [23]. The total energy density must greatly exceed the rest mass energy density of the outflow. In contrast PFDO's can in principle transport large amounts of energy through a vacuum without much matter. Poynting flux driving is a part of a number of models: tori in neutron star mergers [19, 30, 18, 6], highly magnetized millisecond pulsars [31, 3, 28], and collapsars (e.g. [15, 33]). See also the recent comprehensive study of [13].

For PFDOs, the particle acceleration occurs from dissipation of the magnetic energy. Understanding the physics thereof requires studying relativistic collisionless plasmas. Several mechanisms of PFDO dissipation have been proposed in the literature. Direct dissipation of magnetic energy by fast reconnection has been considered [12, 29, 5, 14]. Alternatively, Ref. [27] modeled the interaction of a strongly magnetized wind with an external medium. In the wind rest frame this scenario is identical to the collision of a wide relativistic cold beam of particles with a strong magnetic barrier. The particle acceleration is driven by electromagnetic fields induced from charge separation between protons and electrons dragged from the ambient medium by the barrier. Electrons can acquire a substantial fraction of the proton kinetic energy to produce synchrotron emission.

More recently, a new but related acceleration mechanism has been proposed by [10] involving a hot magnetized collisionless plasma, confined to a finite slab (rather than the infinite slab of [27]) and suddenly released into a vacuum. The surface gradient of the magnetic field generates a strong diamagnetic current which shields the interior and confines the field to the expanding plasma, but the initial magnetic slab breaks into multiple pulses. An electric field of order $|E| \sim c|B|$ is associated with the magnetic field of each pulse. Particles are trapped in the pulse surface layer and accelerated to higher and higher energies via the ponderomotive force of the magnetic pressure gradient. This mechanism has been termed the diamagnetic relativistic pulse accelerator (DRPA) by [10].

The wind set-up [27] can be thought of as a special case of a magneto-acoustic pulse in the finite pulse model [10] for which the pulse has an infinite width in the propagation direction. We will demonstrate that the pulse width is particularly important for the interaction with the ambient medium. Depending on whether the width is larger or smaller than the particle gyro-radii there are three general possibilities: (i) the external matter crosses the pulse and is lost to the interior of the expanding plasma, (ii) the external particles get trapped and accelerated inside the pulse or (iii) the external particles are reflected into the oncoming material. (In the relativistic regime, we will see that (ii) and (iii) are largely indistinguishable.)

For realistic pulses, the rise of the magnetic field strength at the leading edge of the leading pulse will be smoother than the abrupt jump assumed in [27] which makes a significant difference. Complementarily, although an ambient medium was included in [9] its effect not yet been thoroughly studied in detail. That is a goal of this work.

In addition to investigating the interaction between the pulse and the ambient medium, we will also study the spectrum of the both the internal and external particles. While many of the particles initially inside the pulse remain trapped, they get accelerated to high energies. This fast population of electrons will emit synchrotron radiation. The interaction of the pulse with the ambient medium can deliver a second delayed contribution to the emission: In cases where the external material gets trapped and accelerated in the pulse, (case *(ii)* above), it is expected that these captured electrons also radiate synchrotron emission. This emission can be delayed with respect to the primary prompt emission if the density of the ambient medium is low compared to the density of the internal matter: a significant time is then needed for electrons to pile up to densities that produce observable radiation. This secondary emission can either blend in with the prompt emission and determine the late evolution therefore can be separated in time and form a completely distinct part of the systems radiation emission.

We tackle the problem of magnetic pulse-ambient medium interaction with fully relativistic PIC simulations. The magnetic pulse width, shape and strength are not assumed, but are generated self-consistently from the driving event, namely the sudden expansion of the strongly magnetized plasma. Unlike previous simulations, we use the real electron proton mass ratio of $m_e/m_p = 1/1836$ (see e.g. [10]).

In Sec. 2 we describe the code used and the simulation set-up. Sec. 3 addresses the basic mechanism of particle reflection at a magnetic pulse and a simple model is presented and compared to simulation results. The long term pulse evolution is discussed in Sec. 4. We discuss the accelerated particle spectrum in Sec. 5. In Sec. 6 we show that the pulses can act as electron selective filters. In Sec. 7 a possible application to GRBs is discussed. We summarize in Sec. 8.

2. Simulation Setup and Code

The basic physical setup is as follows: an initial magnetic field in the z -direction, i.e. $\vec{B}_0 = (0, 0, B_z)$, is placed in a plasma slab of finite thickness at $x = 0$. Due to the magnetic pressure gradient, the slab expands in both the positive and negative x -directions (see Fig. 1). As in [10] we focus on the part of the slab expanding into the $+x$ -direction. Throughout this work, times are normalized to the initial non-relativistic gyro frequency of the internal electrons $\Omega_e^* = eB_0/m_e$.

The code VORPAL [20] used in our simulations is a fully relativistic 3D open source plasma simulation code based on the PIC algorithm presented in [2]. VORPAL can be used in an arbitrary number of phase space dimensions. The simulations herein are referred to as $2\frac{1}{2}$ dimensional, referring to two dimensions in space (see Fig. 1) and three in velocity space. The code is freely available for academic use under a public license agreement. Our simulations are performed on a linux cluster with 8 CPUs dedicated to the computations. We were therefore able to extend single simulation runs over months, resulting in simulation times much longer than in previous analyses.

The PIC algorithm introduces a uniform spatial grid to calculate field quantities. The particles' space and velocity coordinates are continuous, and advance through extrapolation of the field quantities and the resulting forces. The grid spacing

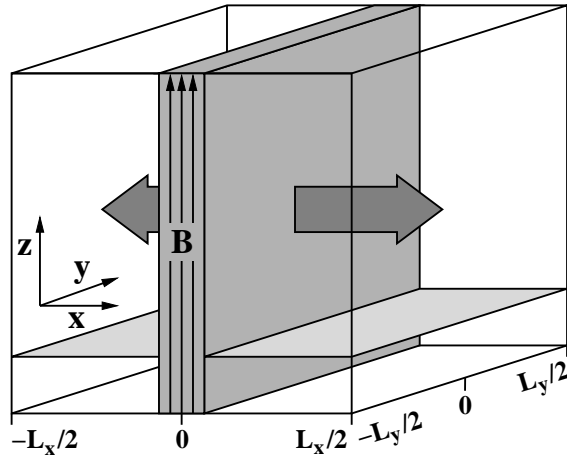


Figure 1. Sketch of the simulation box setup. The initial internal plasma is contained in the central plasma slab which is permeated by a magnetic field. The volume outside the slab is filled with the ISM (shown as transparent for clarity). The light shaded plane is the simulated 2D portion of the volume and the arrows indicate the direction of expansion.

throughout our simulations is given by the inertial length of the initial electrons. $\Delta_x = \Delta_y = \Delta = c/\omega_e \approx 0.0168 \cdot (n_{e,0}^{int}/10^{17} \text{ m}^{-3})^{-1/2} \text{ m}$, where $\omega_e = \sqrt{e^2 n_{e,0}^{int}/\epsilon_0 m_e}$ is the electron plasma frequency defined in the laboratory frame, and $n_{e,0}^{int}$ is the initial internal electron density. The x and y domains are periodic and run from $-L_x/2$ to $+L_x/2$ and $-L_y/2$ to $+L_y/2$ respectively. The magnetic slab initially centered at $x = 0$, expands in the x -direction. Since a magnetic pulse propagates at approximately c , the simulation time-spans are given by the time for light to cross half of the box in the x -direction, i.e. $t \approx (L_x/2)/c$, ensuring that the pulse does not leave the box. The time resolution of the simulation is chosen such that $\Delta t \approx 0.1 \cdot \min[1/\Omega_e, 1/\omega_e]$. All quantities are presented in dimensionless units. The choice of one parameter, e.g. the initial magnetic field, then fixes all other quantities for a given setup. Throughout the following, physical quantities are calculated for an initial magnetic field of $B_0 = 4.473 \text{ T}$.

Plasma particles are treated as macro particles, each corresponding to many real particles. In the simulations herein, each particle species is initially represented by 50 macro particles per cell. Typically millions of particles are simulated. The particle species are indicated by subscripts with the subscript *int* and *ext* indicating particles initially inside or outside of the magnetic slab. These internal and external particles can be further subdivided into electron and ion or electron and positron populations. In the context of a GRB, the external plasma would represent the interstellar medium (ISM). For the external plasma we use $|B_{ext}| = 10^{-10} \text{ T}$, $n_e^{ext} = n_p^{ext} = 10^6 \text{ m}^{-3}$.

Variation of the internal plasma parameters is described below, but particles are always initially loaded with relativistic Maxwellian distribution of temperature T

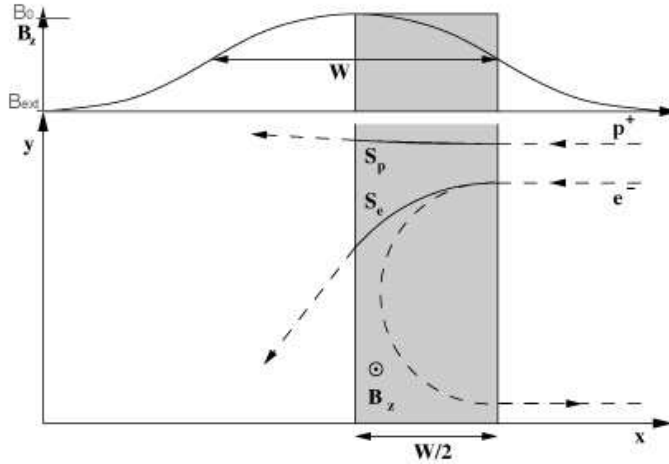


Figure 2. Sketch of external electron and proton motion in the pulse rest frame. The pulse we study is the leading pulse that breaks off from the initial slab. Depending on the pulse width W and its velocity, an incoming electron can either be reflected or transmitted. For the parameter ranges considered, protons are always transmitted. S_p and S_e are the path lengths inside the first half of the pulse for protons and electrons respectively. Only the leading half of the pulse (shaded) matters for assessing transmission or reflection. The magnetic field range is shown from $B = B_{ext}$ at the base of the Gaussian-like field profile, to $B = B_0$ at the apex.

throughout the simulation volume. Unlike previous authors who invoked a reduced mass ratio $m_p/m_e = 100$ [22], we use the actual ratio of $m_p/m_e = 1836$.

3. Particle transmission, reflection, and trapping

Including a finite density ambient medium in the DRPA process allows the interaction between the slab and ambient medium to be studied. Early simulations with $\beta_{int} \geq 0.1$ (where $\beta = 2\mu_0 n_e k_B T_e / B_0^2$), suggested that external material is neither reflected nor piled up ahead of the pulse, whereas simulations with initially low β show a pile-up of external electrons. Due to the high degree of relativity, reflection and trapping of external particles are not distinguishable in the lab frame. Particles cannot propagate ahead of the pulse significantly, and stay close to its front like trapped particles. Reflection and trapping will thus be used synonymously below.

3.1. Transmission vs. reflection: the basic picture

Our simulations are performed in the laboratory frame where the mean initial velocity of all particle species vanishes. In order to analyze the conditions for transmission vs. reflection of external material it is convenient to transform the simulation results into the pulse rest frame. Below, un-primed quantities refer to values measured in the rest frame and primed quantities are in the laboratory frame.

From Ohm's law, the perpendicular electric field in the pulse vanishes in its rest frame. External particles penetrate the pulse as a cold beam with speed $v_{ext} = -v_{pulse}$.

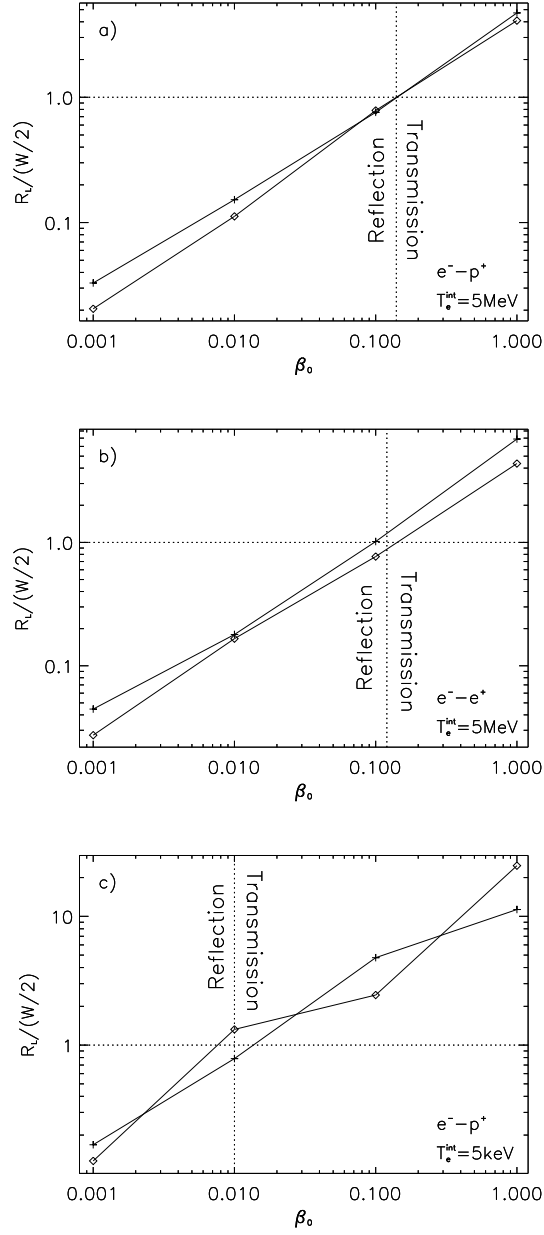


Figure 3. Ratio of Larmor radius R_L of the external electrons inside the pulse to $W/2$, the HWHM value of the pulse measured in the pulse rest frame. The plots a) and b) show the simulation results for an initial temperature of 5 MeV for an $e^- - p^+$ and an $e^- - e^+$ internal plasma while plot c) shows results for an $e^- - e^+$ internal plasma with initial temperature of 5 keV (open squares are lower density case; crosses are higher density case).

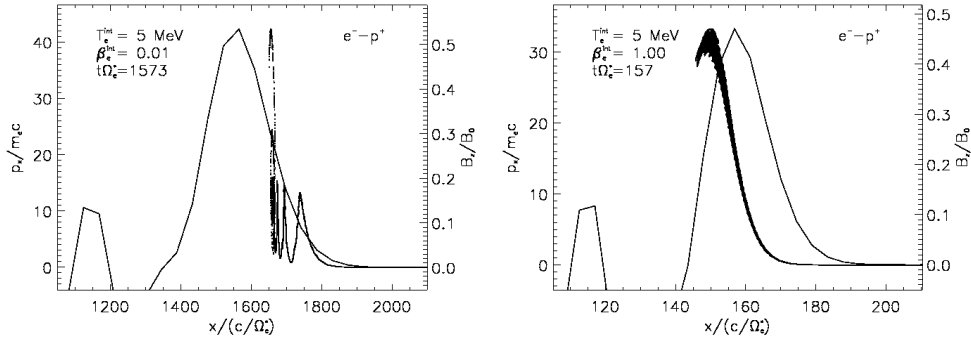


Figure 4. Phase space plot of the external electrons with over plotted magnetic field profile in the laboratory frame. Electron-proton plasmas at a temperature of $T_e = T_p = 5\text{MeV}$ are displayed. On the left hand side the initial internal plasma beta is $\beta_e^{\text{int}} = 0.01$, a value at which electron reflection is expected according to Fig. 3. On the right hand side an initial plasma beta of $\beta_e^{\text{int}} = 1.00$ is depicted. The times in the evolution of the system have been chosen to be equal in real time.

The relativistic gyro-frequency for an incoming particle of species α in the pulse rest frame is therefore given by

$$\Omega_\alpha^{\text{ext}} = \frac{q_\alpha B}{m_\alpha \Gamma_{\text{pulse}} c} \quad , \quad (1)$$

where $\Gamma_{\text{pulse}} = 1/\sqrt{1 - v_{\text{pulse}}^2/c^2}$ is the Lorentz factor of the pulse in the laboratory frame. The pulse magnetic field in the rest frame is $B = B'/\Gamma_{\text{pulse}}$, where B' is the magnetic field in the laboratory frame.

Figure 2 shows the situation in the pulse frame. In assessing whether or not a particle is reflected, only its trajectory in the leading half of the pulse matters. Analyzing whether a particle will reflect is simplified by approximating the leading half of the pulse profile by a magnetic field filling a rectangular area of width $W/2$ (gray shaded area in Fig. 2). As seen from the sketch, reflection requires the half-pulse width to exceed the Larmor radius.

Ref. [21] showed that the width W of the leading pulse that breaks off from the slab scales as the width of the initial slab. Fig. 2 shows that the larger the pulse width is compared to the external particle's gyro-radius, the more likely that particle will reflect. Ref. ([27] considered an essentially infinite pulse, and accordingly, particles are all reflected).

The pulse shape is not maintained over long times [9] and instead bifurcates into a complex structure of multiple peaks. The sub-pulses have widths of order $\sim 10c/\omega_e$ and are otherwise independent of the initial plasma properties. Even if the leading pulse is too large to allow particle transmission, the ultimate reflection or transmission is determined by the behavior of smaller sub-pulses in a later phase of the pulse evolution. Because computational limits are prohibitive, early development of small pulses must be created by choosing a small enough initial plasma slab.

3.2. Numerical study of parameters influencing reflection vs. transmission

The results of our simulations confirming the basic condition for reflection are shown in Fig. 3. We used two different temperatures $T_e^{\text{int}} = T_p^{\text{int}} = 5 \text{ keV}, 5 \text{ MeV}$ and four values of the internal electron-to-magnetic pressure ratio $\beta_e^{\text{int}} = 0.001, 0.01, 0.1, 1.0$. The internal density was varied by a factor of four for each choice of β_e^{int} . The width of the initial slab W_s is held constant between runs so such that $W_s = 6 c/\omega_e^{\text{low}} = 12 c/\omega_e^{\text{high}}$ in grid spacing units, where 'high' and 'low' refer to the corresponding density cases. We used an initial external plasma composition of $e^- - p^+$ and internal plasma compositions of either $e^- - p^+$ or $e^- - e^+$.

The simulation box dimensions are $L_x = 500 c/\omega_e$ and $L_y = 80 c/\omega_e$. The initial plasma beta is $\beta_e^{\text{int}} = 0.01$ and the simulations cover a timespan of $\Omega_e^* t \approx 11025$.

By measuring the lab frame pulse velocity, field strength, and width, we obtain the corresponding values in the pulse rest frame. Comparison of the electron Larmor radius with the pulse width yields the data of Fig. 3. The results of the $e^- - p^+$ and the $e^- - e^+$ simulations at temperatures of 5 MeV and 5 keV are shown. Values of $R_L/(W/2) < 1$ indicate that electrons should be reflected while $R_L/(W/2) > 1$ show the transmission of external electrons to the internal material downstream of the pulse. As can be seen from the $e^- - p^+$ simulations, the transition value roughly scales with the plasma temperature.

The high temperature $e^- - e^+$ results are as clean as the $e^- - p^+$ case. The critical R_L marking the transition from reflection to transmission is the same as in the $e^- - p^+$ case. In contrast, the transition between reflection and transmission in the low temperature $e^- - e^+$ simulations is hard to pinpoint because the pulse structure is more quickly influenced by the pick-up of external electrons. Counter streaming currents perpendicular to the pulse velocity drive instabilities, causing the pulse to fragment early. For an $e^- - p^+$ plasma, trapping of electrons has much less effect on the overall pulse structure on the same time-scales.

The initial plasma density has little influence on the results in Fig. 3a-c. The transition value of the initial β_0 therefore scales primarily with the plasma temperature. The lower the temperature the lower the limiting β_0 .

The linear dependence of $R_L/(W/2)$ on β_0 as shown in Fig. 3a-c is not strictly valid on all scales. Extending the analysis to very small magnetic field strengths leads to a break down of the linearity. In the case of large magnetic fields, however, the linear dependence is observed in all simulations. More work is needed to systematically understand the dependence for much larger and much smaller field strengths.

The observed linear dependence of $R_L/(W/2)$ on β_0 allows us to derive a scaling for the pulse Lorentz factor Γ_{Pulse} in the present parameter region. Using $W \propto c/\omega_e$ and the definition of R_L with $R_L/(W/2) \propto \beta_0$ we find the following scaling of the pulse Lorentz factor

$$\Gamma_{\text{Pulse}} \propto \frac{n_e^{1/2} T_e}{B_0} . \quad (2)$$

This equation is valid under the assumption that the density of the ambient medium is small enough not to influence the pulse propagation.

3.3. Phase space analysis of trapping/reflection

Figure 4 illustrates the differences in pulse-particle interaction for the cases of transmission vs. trapping: Fig. 4a shows the external electron phase plot $x - p_x$

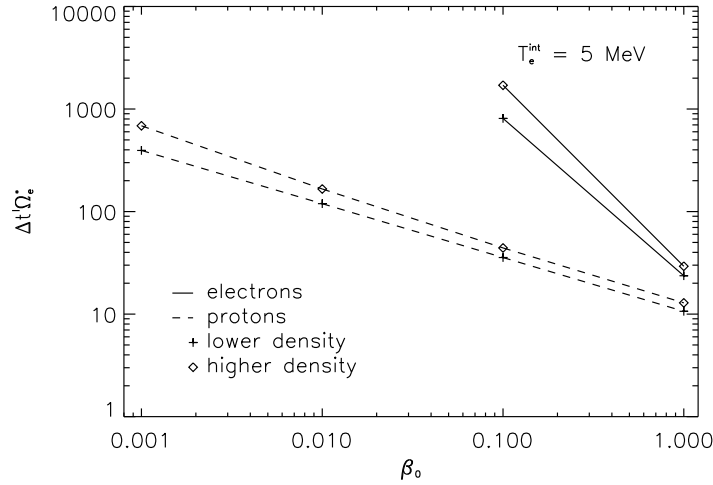


Figure 5. Time needed for electrons and protons to cross the pulse in the laboratory frame. The electron solutions do not exist for $\beta_e < 0.1$ since $R_L^e < W/2$ and the particles cannot cross the pulse. Since $R_L^p \gg W/2$, the proton solutions in this regime correspond to the pulse crossing time for a free flying particle.

superimposed on the magnetic field profile of the pulse in the laboratory frame for an initial $\beta_e^{\text{int}} = 0.01$, a value for which reflection/trapping is expected. As shown, the external electrons pile up at the pulse. In contrast, Fig. 4b shows the analogous plot for $\beta_e^{\text{int}} = 1.0$. Here transmission is expected and seen.

3.4. Electron and proton pulse crossing times

Electrons take longer to cross the pulse than the protons. To show this, we first define the pulse crossing time as that needed to travel half the pulse width $W/2$. In the rest frame, the particle propagates in the $-x$ direction with Lorentz factor $\Gamma_{\text{pulse}} = 1/\sqrt{1 - (v_{\text{pulse}}/c)^2}$. The space-time event of the pulse encounter occurs at (t_1, x_1) and the event of exit is at $(t_2, x_2) = (t_1 + \Delta t, x_1 - W/2)$ (Note: x_2 is given by $x_2 = x_1 - W/2$), where Δt is the time spent inside the pulse. The time interval in the laboratory frame is then given by

$$\Delta t' = t_2' - t_1' \quad (3)$$

$$= \left[\left(t_2 + \frac{|v_{\text{pulse}}|x_2}{c^2} \right) - \left(t_1 + \frac{|v_{\text{pulse}}|x_1}{c^2} \right) \right] \Gamma_{\text{pulse}}, \quad (4)$$

resulting in

$$\Delta t' = \Gamma_{\text{pulse}} \left(\Delta t - \frac{v_{\text{pulse}}}{c^2} W/2 \right) . \quad (5)$$

For protons, the pulse width is much smaller than the gyro radius and the trajectory is approximately a straight line. The path length then equals the pulse width so the time spent inside the pulse is $\Delta t \approx (W/2)/v_{\text{pulse}}$. Then Eq. (5) reduces to $\Delta t' \approx \Delta t/\Gamma_{\text{pulse}}$.

The time spent in the pulse for particles (like intermediate energy electrons) with

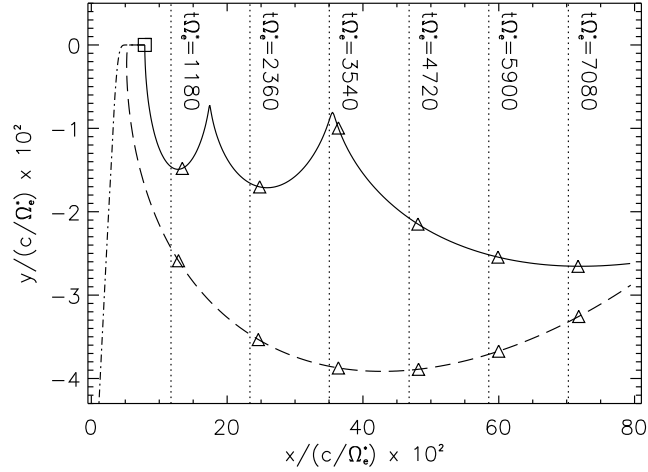


Figure 6. Electron trajectories for electrons encountering the EM pulse at three different initial velocities in the $-x$ direction. The solid line corresponds to zero initial velocity, the dashed line to $\gamma_e \sim 1.6$ and the dash-dotted line to $\gamma_e \sim 117$. Triangles indicate particle positions at given times along the trajectories and dotted vertical lines are the positions of the moving pulse. All particles start at the position indicated by a square. The vertical dotted line represents the pulse location at the times indicated.

finite curvature trajectories is

$$\Delta t = \Delta t = \alpha_0 / \Omega_\alpha^{\text{ext}} = \frac{\arcsin\left(\frac{W}{2R_L^e}\right)}{\Omega_\alpha^{\text{ext}}}, \quad (6)$$

where α_0 is the angle of particle gyration.

For a proton with $R_L^p \gg W$ the path length inside the pulse is given by $S_p \approx W$, whereas electrons with $R_L^e \sim W$ have $S_e > W$. Because both protons and electrons move with approximately the same speed $\sim c$, electrons spend more time inside the pulse. The pulse crossing will therefore be observed later for electrons than for protons. Figure 5 shows the expected time delays in the laboratory frame for the simple model of pulse particle encounter depicted in Fig. 2 by using Eqs. (5) and (6). The expected delays between electrons and protons agree with measured results from the simulations to within a factor of 2.

3.5. Tracking single electron trajectories

In the laboratory frame (which is the simulation frame), the pulse also contains an electric field, $\vec{E}' = (0, E'_y, 0)$, perpendicular to the direction of expansion and to the magnetic field. The electric field strength is given by $E'_y \sim v_{\text{pulse}} B'_z$. Electrons entering the pulse's EM field therefore experience an $\vec{E}' \times \vec{B}'$ - drift in the $+x$ -direction. This drift velocity equals the pulse velocity so the particles are carried with the pulse.

To track a single particle in PIC simulations and test for the influence of the drift force, we define it as its own species and add it to the simulation. By varying the initial velocity of the single particle while keeping everything else the same, we can

mimic different pulse velocities and compare the resulting particle trajectories. We use an initial $\beta_e^{\text{int}} = 0.01$ and a temperature of $T_e^{\text{int}} = T_p^{\text{int}} = 5$ MeV.

The trajectories for electrons with three different initial velocities are displayed in Fig. 6. We take the internal plasma to be a proton-electron plasma. The fastest electron corresponds to the case of transmission described in the preceding section. As the electron enters the EM field of the pulse it is subject to the drift force just discussed and an electric force in the y-direction. After a partial gyration, the particle leaves the pulse downstream.

The simulation with the electron initially at rest corresponds to an cold ambient electron encountering the pulse. The particle starts gyrating and experiences an $\vec{E}' \times \vec{B}'$ - drift which drags it along the front of the pulse.

The electron with the intermediate quasi-relativistic velocity has a nearly open trajectory, and is not able to perform a full gyration during the transit shown. Although it appears to stay a constant distance ahead of the pulse (triangles in Fig. 6), comparing the particle Lorentz factor with that of the pulse reveals that the electrons are actually moving faster than the pulse but moving toward it.

For the intermediate velocity electron, the peak Lorentz factor $\gamma_{\text{max}}^{\text{med}} \approx 82$ and for the zero initial velocity electron it is $\gamma_{\text{max}}^{\text{zero}} \approx 42$. Both values peak when the electron velocity is aligned with the pulse velocity. The pulse Lorentz factor at this time is around $\gamma_{\text{max}}^{\text{pulse}} \approx 12$.

4. Long term evolution

Here we take an e^-e^+ internal plasma and an e^-p^+ external plasma. The simulation box size for this simulation is $L_x = 8000\Delta$, $L_y = 10\Delta$. For an initial plasma beta of $\beta_e^{\text{int}} = 0.01$ at a temperature of $T_e^{\text{int}} = 5$ MeV we can follow the pulse evolution up to a time of $t\Omega_e^* \sim 157000$ (compared to $t\Omega_e^* \sim 10^4$ in the previous section).

4.1. Long term energetics

The total energy of fields and particle species are displayed in Fig. 7. As described in Ref. [10], an initial static magnetic field results in two electromagnetic pulses propagating in opposite directions into the surrounding volume. Due to the plasma expansion, the energy in the magnetic field rapidly decreases and is transferred to a growing electric field of $E_y \sim v_{\text{pulse}}B_z$ until an equipartition value in the field energy is reached. This energy transfer happens in the first $\sim 150 \Omega_e^*t$. After that, the internal particles gain significant energy. Internal electrons and positrons experience the same energy increase and are plotted as one line in Fig. 7. The external electrons gain energy right from the start of the expansion. Due to the low ambient particle density (i.e. the ISM), its energy content is small and in order to be visible in Fig. 7 we have scaled it by a factor of 10^8 . The internal particles continuously gain energy until $\Omega_e^*t \approx 8000$. At this point the total particle energy starts to decrease and the electromagnetic field regains energy. Such behavior has also been observed in Run D of [21] but the subsequent evolution was not followed there.

In the long term evolution seen in Fig. 7, the energy exchange between internal particles and the electromagnetic field is somewhat oscillatory in time. Although the total energy of the entire particle population can decrease due to particle leakage, the energy in the trapped particles still rises [10]. As a measure of their energization, we

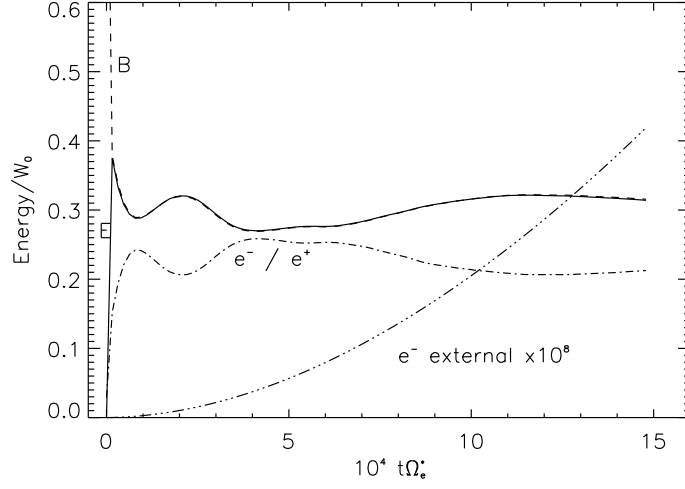


Figure 7. Energy evolution of the system: total magnetic field energy, total electric field energy and total internal electron/positron and total external electron energies (enhanced by a factor of 10^8) are shown. All energies are normalized to the initial magnetic field energy M_0 .

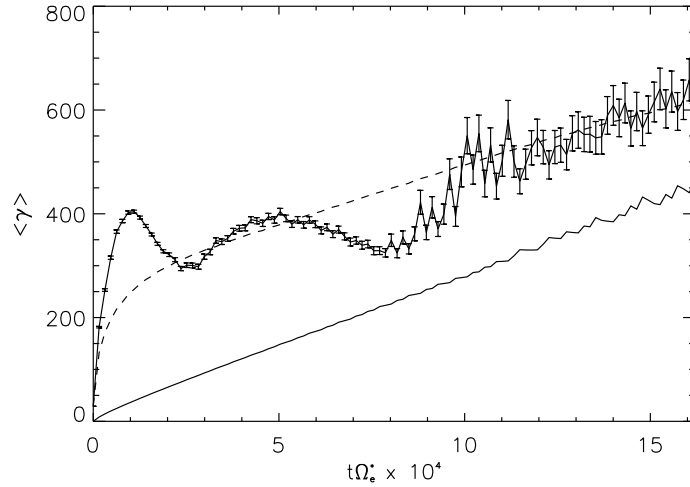


Figure 8. Mean Lorentz factor $\langle \gamma \rangle$ of the internal electrons (upper solid line with error bars) and external electrons (lower solid line) vs. time. The dashed line represents the fit of Eq. (8) to the internal data and the error bars are the standard error of the mean. The fit parameters are $f = 9.80$ and $C_0 = 927.96$.

show the evolution of the mean Lorentz factors

$$\langle \gamma(t) \rangle = \frac{\int_{\text{pulse}} N(\gamma(t)) \gamma(t) d\gamma}{\int_{\text{pulse}} N(\gamma(t)) d\gamma} \quad (7)$$

of the internal/external electron population as a function of time in Fig. 8. For internal particles, the integrations in Eq. (7) extend over all electrons in the leading pulse and for external electrons, the integration is over a surface layer of thickness $\sim 12 c/\omega_e$ upstream of the pulse.

The mean energy gain for electrons inside the pulse has been derived analytically to obey [9]

$$\langle \gamma(t) \rangle = \sqrt{2f\Omega_e(t)t + C_0} \quad , \quad (8)$$

where C_0 and f are constants that depend on the initial plasma conditions and $\Omega_e(t)$ is the non-relativistic instantaneous gyro frequency. Though only co-moving electrons are assumed in the derivation of Eq. (8) $\langle \gamma(t) \rangle$ this is not the pulse Lorentz factor. The latter is determined by averaging *before* squaring, namely $\Gamma_{\text{pulse}} = 1/\sqrt{1 - \langle \beta_x \rangle^2}$. This gives comparable results to the magnetic peak velocity shown in Fig. 9c. Our interpretation of Eq. (8) therefore differs from that of [9].

At early times, large deviations from the theoretically predicted time dependence are observed (Figure 8). This is due to the assumptions made in the derivation of Eq. (8). The fit parameter f , which is assumed to be constant in time, includes the averaged pulse profile. The pulse shape, however, changes during the evolution of the system and f is expected to change with time. For example, the deviation from Eq. (8) at $t\Omega_e^* \approx 8 \cdot 10^4$ in Fig. 8 is caused by the coalescence of the leading pulse with a trailing pulse, which suddenly increases the pulse width (see Fig. 9b).

A full analysis of the energy evolution requires consideration of energy losses due to radiation. An estimate of the synchrotron loss-time yields

$$t_{\text{syn}} \approx 10^{-7} \text{ s} \left(\frac{100}{\gamma_e} \right) \left(\frac{10^3 \text{ T}}{B_z} \right)^2 \quad . \quad (9)$$

Using $B_z \sim 1$ T and assuming a Lorentz factor $\gamma_e \sim 10^4$ yields $t_{\text{syn}} \approx 10^{-3}$ s. Synchrotron losses are therefore not relevant for the duration of the simulation presented herein and can be neglected. However, we will later consider them in the extrapolation to late times.

4.2. Long term pulse evolution

The evolution of the pulse is important for acceleration of the external particles. The pulse width, peak magnetic field and velocity determine whether the pulse will reflect, trap, or transmit the ambient particles.

The three key pulse properties are displayed in Fig. 9. Only the leading pulse is considered since its values determine the interaction at the outermost interface with the ambient plasma (the peak magnetic field plotted is only that of the leading sub-pulse, not the global maximum). Figure 9a shows the decay of the peak magnetic field of the leading pulse. The dashed line displays the line of a logarithmic decay of the form $f(t) = 1 - C_0 \log C_1 t$. The pulse evolution follows this formula for $\Omega_e^* t \approx 3 \cdot 10^4$. For later times, the peak magnetic field of the pulse stabilizes and seems to asymptotically approach of $|B_z|/B_0 \approx 0.12$.

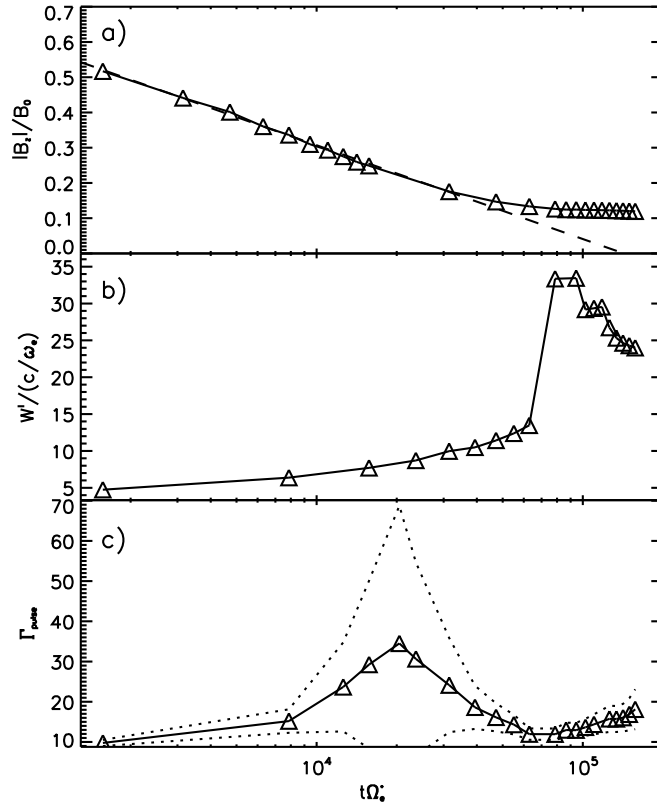


Figure 9. Pulse evolution in the course of the longterm simulation. Panel *a*) shows the maximum magnetic field of the leading peak (not necessarily the maximum of all peaks in the whole pulse). The pulse width W' in the laboratory frame is displayed in panel *b*) and the pulse Lorentz factor derived from the peak position in time is displayed in panel *c*). The dotted lines show the error margin.

Figure 9b shows the time evolution of the pulse width W , defined as the FWHM value. The pulse exhibits a continuous broadening until a time $\Omega_e^* t \approx 7 \cdot 10^4$ where a jump occurs. The sudden change is due to coalescence of a trailing sub-pulse with the leading pulse. Predicting the longer term pulse width evolution is difficult but we can estimate that, to order of magnitude, $W \sim 10c/\omega_e$. This is consistent with the $\sim \Gamma_{\text{pulse}}c/\omega_e$ estimate in [9] and the pulse velocities shown in panel *c*) of Fig. 9.

The Lorentz factor of the leading pulse is displayed in Fig. 9c. The pulse velocity has been determined by fitting a Gaussian to the uppermost peak where the pulse is closest to being symmetric. The position of the centroid at the corresponding times then yields the pulse velocity. Starting at $\Gamma_{\text{pulse}} \approx 10$, the pulse reaches a peak of $\Gamma_{\text{pulse}} \approx 35$ and decelerates later to a value of $\Gamma_{\text{pulse}} \approx 12$. Toward the end of the simulation, the pulse gains speed and ends up with $\Gamma_{\text{pulse}} \approx 19$. The low Lorentz factors at times around $7 \cdot 10^4 \Omega_e^* t$ derive from the coalescence of the leading pulse with a trailing pulse (see the jump at the same time in panel *b*) of Fig. 9).

So, at the latest times, the peak magnetic field strength is given by a nearly

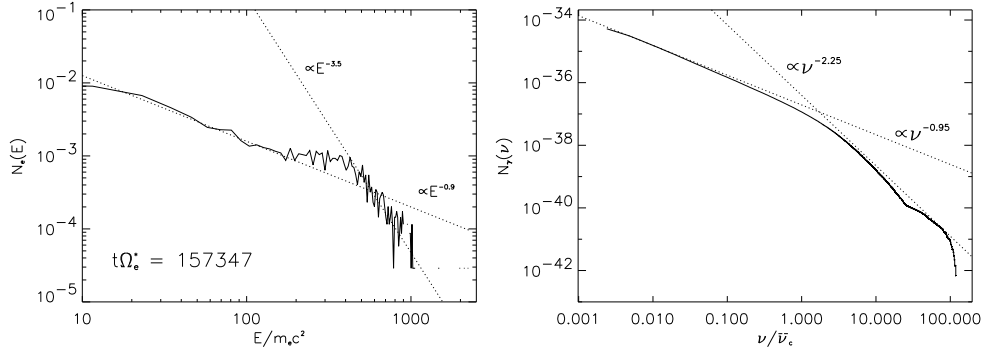


Figure 10. Left: The energy spectrum of the internal electrons at a time of $\Omega_e^* t = 157347$. Two sections of the spectrum are fit by power-laws with slopes $\delta = 0.9$ at low energies and $\delta = 3.5$ at high energies. **Right:** Photon number density vs. frequency. The frequency is normalized to the critical frequency $\bar{\nu}_c = \bar{\nu}_c(\bar{\gamma}, B)$ (Equation 10) with $\bar{\gamma} = \langle \gamma_e^{\text{int}} \rangle$ and B is the peak magnetic field in the pulse. The dotted lines display the slopes expected from Eq. (19). The spectrum computed from the particle distribution produced by the simulation is shown by the solid line.

constant $|B_z|/B_0 \approx 0.12$. the pulse width seems to remain close to $W' \approx 10c/\omega_e$, and $\Gamma_{\text{pulse}} \approx 15$.

5. Radiation spectra

Highly energetic electrons moving in magnetic fields generate electromagnetic radiation. In the following we derive and discuss the radiation spectra that are expected to be produced by the DRPA. The spectra are obtained from a given electron energy distribution in our simulations and an emission model, e.g. synchrotron emission. A different approach can be found in [?] where the emitted radiation is self-consistently computed.

5.1. Synchrotron vs. jitter

Due to the large electron Lorentz factors the radiation is beamed into a narrow cone with opening angle $\Delta\theta \sim 1/\gamma$. Two different types of radiation can emerge: 1) synchrotron radiation [25] and 2) 'jitter' radiation [16]. For synchrotron radiation the characteristic emission frequency is determined by the particles gyration on a circular orbit. The emitted radiation beamed in to $\Delta\theta$ is directed toward the observer only for a short fraction of the gyration. The radiation is pulsed with a typical duration $\tau_p \sim 1/\omega_e$. Thus, the emission frequency is determined by the particle gyro frequency and the exact expression is given by (e.g. [11])

$$\nu_c^{\text{sync}} = \frac{3}{2}\nu_e\gamma^2 = \frac{3eB\gamma^2}{4\pi m_e} \quad , \quad (10)$$

where $\nu_e = \Omega_e/2\pi = eB/2\pi m_e$.

Jitter radiation occurs if the observer always remains in the beam of the emission from the radiating particle. The particle motion can be deflected by small-scale (smaller than the particle gyro radius) fluctuations in the magnetic field, resulting

in a random scattering of the particle trajectory. But if the deflections are small, and if the beam angle is larger than the pitch angle, the radiation beam always points toward the observer. Modulation occurs with a frequency determined by the scale length of the inhomogeneities of the magnetic field and the particle velocity. The characteristic emission frequency is

$$\nu_c^{\text{jitter}} = \frac{\gamma^2 c}{\lambda} \quad , \quad (11)$$

where λ is the scale length of the magnetic field inhomogeneities.

The characteristic quantity which determines the dominant emission process is the ratio between the angle of gyration a particle performs on a scale length of the magnetic field, α_0 , and the opening angle of emission $\Delta\theta$, i.e. $\delta \sim \alpha_0/\Delta\theta$ [16]: for $\delta > 1$ the emission is synchrotron and 'jitter' otherwise. Using Eq. (6), the condition for 'jitter' radiation is equivalent to

$$\lambda < \frac{c}{\Omega_e} \quad . \quad (12)$$

This condition is independent of the particle velocity. The typical length scale of the magnetic inhomogeneities in the magnetic pulse, i.e. the sub-pulses due to fractionation, are of the order of a few $\Gamma_{\text{pulse}}c/\omega_e$, hence

$$\lambda_{\text{DRPA}} \sim \frac{\Gamma_{\text{pulse}}c}{\omega_e} = \frac{c}{\Omega_e} \Gamma_{\text{pulse}} \left(\frac{\Omega_e}{\omega_e} \right) \quad . \quad (13)$$

Since our plasma is magnetically dominated $\Omega_e/\omega_e > 1$ and we find $\lambda_{\text{DRPA}} > c/\Omega_e$.

We therefore conclude that the dominant radiation process for electromagnetic radiation from the DRPA is synchrotron emission. This conclusion differs from that of [9] where 'jitter' radiation was assumed.

5.2. Synchrotron radiation spectra

The energy loss dE/dt resulting from synchrotron radiation is given by (e.g. [11])

$$\frac{dE}{dt} = \frac{e^2 \gamma^4}{6\pi\epsilon_0 c^3} \left(\left(\vec{E} + \vec{v} \times \vec{B} \right)^2 - \left(\vec{E} \cdot \vec{v} \right)^2 \right) \cdot \gamma^2 \quad . \quad (14)$$

When \vec{E} is ignored, the spectral intensity is then

$$I_\nu = \frac{\sqrt{3}e^3 B \sin(\alpha_p)}{4\pi\epsilon_0 m_e c} F(x) \quad (15)$$

where

$$F(x) = x \int_x^\infty K_{5/3}(z) dz, \quad (16)$$

and $K_{5/3}(z)$ the modified Bessel function of order 5/3. The argument $x = \nu/\nu_c$ is the ratio of frequency over the critical frequency (Equation 10). The equations can be simplified for $\vec{v} \cdot \vec{B} = 0$, a reasonable assumption in our case since $\vec{B} = (0, 0, B_z)$, and particles are mainly energized in the x,y-direction.

The energy loss for a single electron averaged over all pitch-angles is then given by [11]

$$-\left(\frac{dE}{dt} \right) = \frac{4}{3} \sigma_T c U_B \beta^2 \gamma^2, \quad (17)$$

where σ_T is the Thompson cross section, and $U_B = B^2/2\mu_0$ is the magnetic energy density. In the relativistic limit $\gamma \gg 1$ the normalized velocity $\beta = v/c$ can be set to unity.

The emission spectra are computed by summing Eq. (15) over all particles. The resulting spectra are compared to the analytic model spectra for particle energy distribution functions of the form

$$N_e(E) dE = C_e \cdot E^{-\delta} dE, \quad (18)$$

where δ is typically positive, and takes constant values over a finite energy range. This power law translates into photon number density of the form [25]

$$N_\gamma(\nu) = C_\gamma \cdot \nu^{-\tau}, \quad (19)$$

where τ is given by $\tau = (s + 1)/2$.

5.3. Radiation from internal particles

At the latest times in our simulations, the internal particle energy spectrum can be approximated by a double power-law. Here we will assume isotropic particle distributions. This is satisfied for the internal electrons: Although the trapped electrons get anisotropically accelerated, the pulse fractionates at late times, randomizing the magnetic field and thus the particle velocities. At the end of the simulation run, when the photon spectrum is computed, the particle distribution has been roughly isotropized. The internal electron energy spectrum at the end of the long term simulation run is shown in Fig. 10. The region below $E \approx 200 m_e c^2$ is well fit by a power-law with spectral index $\delta \approx 0.9$ while for $E \geq 400 m_e c^2$ we find $\delta \approx 3.5$. An excess of particles is observed at the transition which might be interpreted as another power-law with very small slope.

According to Eq. (19), a double power-law dependence is also expected in the photon number spectrum with index $\tau \approx 0.95$ at lower energies and $\tau \approx 2.25$ above the break spectrum. Summing the contributions from all internal electrons using Eqs. (15) and (10) yields the photon spectrum shown in Fig. 10. The analytically predicted slopes are shown as dotted lines. They agree well with the actual spectra computed from the particle distributions produced by the simulation, although at lower frequencies, the spectrum exhibits a slope of $\tau \approx 1.05$ rather than the predicted $\tau \approx 0.95$. At higher energies, $\tau \approx 2.25$ as predicted. At high energies there is a hump in the spectrum which comes from a fast population of electrons visible as small dots around an energy of $E \sim 2000 m_e c^2$ in Fig. 10. These particles do not fit into the high energy part of the power-law. Only very few particles reach the highest energies and due to limited statistics it is difficult to make conclusive statements about them.

5.4. Saturation and termination of internal electron acceleration

Energy is continuously transferred from the pulse magnetic field into the internal electrons. Some of the energy is radiated away by the electrons. Here we estimate the associated time scale and energies for which these processes balance.

A net energy build-up in the internal electrons only occurs if the energy gain rate exceeds the loss. But the system will eventually reach a steady-state where the energy input balances the energy output by radiation. Knowing the mean acceleration rates of the DRPA and assuming synchrotron emission to be the dominant loss, the time and energy scale to reach saturation can be estimated. The mean acceleration rate

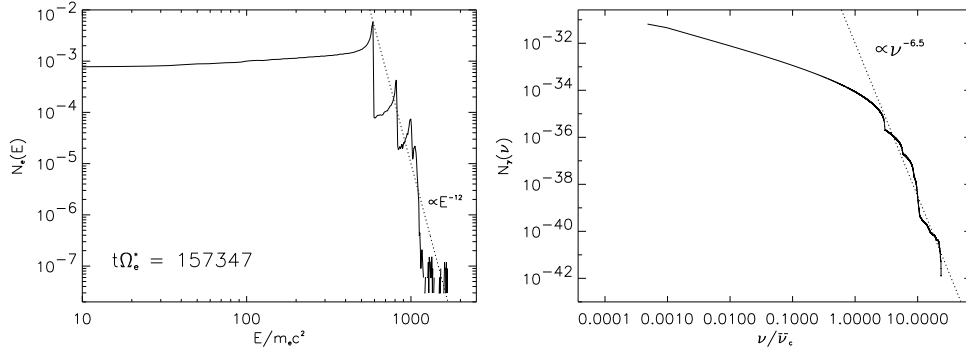


Figure 11. Left: The energy distribution of the external electrons at a time of $\Omega_e^* t = 157347$. The dotted line is the slope in the particle distribution that corresponds to the slope that fits the photon spectrum in the right panel. **Right:** Photon spectrum produced by the external electrons in a thin layer ahead of the pulse. The x-axis normalization is the same as described in the caption of Fig. 10.

of the internal electrons can be obtained via $\frac{d\langle E \rangle}{dt} \Big|_{ac} = m_e c^2 \frac{d\langle \gamma \rangle}{dt}$. Using Eq. (8) and values of f and C_0 obtained from fits to the simulation data in this expression and equating to the synchrotron loss-rate from Eq. (17). Comparison of the mean γ^2 and the square of the mean γ in the simulated electron distribution yields $\langle \gamma^2 \rangle \approx \langle \gamma \rangle^2$ within a factor of 1.5. We can therefore write

$$\Omega_e^* t_{\text{bal}} = \frac{1}{2f\rho} \left[\left(\frac{3}{2} \frac{\mu_0 e c f}{\sigma_T \rho B_0} \right)^{\frac{2}{3}} - C_0 \right], \quad (20)$$

where $\rho \equiv |B_z(t)|/B_0$, assumed to be a constant (~ 0.12) for times $t\Omega_e^* \geq 10^5$ (see Fig. 9a). Equation (20) gives the time-scale for saturation of the DRPA. Using our initial simulation parameters, we find a saturation time of $t_{\text{bal}} \approx 0.0005$ s. The mean electron energy reached at t_{bal} is $\langle \gamma(t_{\text{bal}}) \rangle \approx 3 \cdot 10^4$ resulting in a synchrotron photon energy $E_\gamma \approx 100$ keV. This energy can be corrected to larger values due to underestimating $\langle \gamma^2 \rangle$ in Eq. (20).

5.5. Radiation from external particles

The energy distribution function of the external electrons piled up ahead of the pulse is primarily shaped by the particles' gyration as they encounter the pulse magnetic field. As seen in Fig. 11, the collective gyration creates strong spikes in the energy distribution.

Summing the contributions to synchrotron emission from all external particles using Eqs. (15) and (10) yields the photon spectrum displayed in Fig. 11. The resulting slope at high energies is $\tau = 6.5$. The corresponding slope in the particle energy distribution according to Eqs. (18) and (19) is shown as dotted line in Fig. 11. Such a steep slope is not observed in any phase of the GRB emission, but our simulations cover at most only a microsecond of a real burst. At such times, the density of the external particles accumulated is too low to produce any observable radiation. Only after the prompt emission would the accelerated external population contribute to observable emission. The external particle spectrum is likely to change significantly by then.

Although the energy distribution of the electrons exhibits strong population inversions, no instabilities are observed during the simulation time-span. A two-stream like instability might be expected due to the gyrating beam creating many counter streaming micro-beams in close vicinity to the pulse upstream. The reason the absence of instabilities lies in the highly relativistic nature of the system. Ref. [17] calculates the maximum growth rate for e.g. the magnetic Weibel instability [32]. For a small thermal spread compared to the bulk motion of the beams ($\Gamma_b \approx \Gamma_{b\parallel}$ and $\Gamma_{b\perp} \ll \Gamma_b$, where Γ_b is the total Lorentz factor of the streaming electrons and $\Gamma_{b\parallel,\perp}$ are the parallel and perpendicular components), the maximum growth g_{\max} rate is given by

$$g_{\max}^2 \approx \frac{\omega_e^2}{\Gamma_b} \left(1 - 2\sqrt{2} \frac{\Gamma_{b\perp}}{\Gamma_b} \right) . \quad (21)$$

For large Γ_b the growth rate becomes small.

5.6. Further discussion of the photon spectra and limitations of our calculations

Using the particle energy distribution functions from the simulations to compute the synchrotron spectra requires several approximations. As pointed out in Sect. 5 it is assumed that $\vec{v}_e \perp \vec{B}$, which allows us to ignore the angular correction factor $\sin(\alpha_p)$ in Eq. (15). Also, the magnetic field in the emission region is assumed to be constant and its magnitude is given by the peak value in the pulse.

To compare the analytical results in Eq. (19) with the simulations, we also assumed the particle velocity distribution to be isotropic which can be justified for internal electrons, as discussed earlier. We therefore observe a good agreement between the analytically obtained results for the internal power-law index in Eq. (19) and the power-law index obtained from numerically summing the contribution of each electron (see Fig. 10). External reflected particles, however, are not isotropized on the time scales covered by the simulations. The external electrons do not reach the region of randomized magnetic fields and therefore maintain their anisotropy beyond the end of our simulation. The dotted lines in Figs. 11 and 11 are therefore plotted only to guide the eye and do not have the same robustness as for internal particles.

Do the photon spectra remain stable at late times? For internal electrons, the simulations suggests little change when the radiation loss is unimportant. This follows because the internal electron power law slopes displayed in Fig. 10 do not change during the last third of our simulation run. The spectrum from the external electrons exhibits a power-law index at high energies of $\tau \approx -6.5$ which is rather steep. But even at the end of the simulation, the density of the external particles is too low to produce observable radiation. In contrast to the photon spectrum from internal electrons, that from the external electrons will likely change with time: The external particles in the rest frame of the pulse penetrate the region of magnetic field as a relativistic cold beam. The collective gyration of these particles produces spikes in the electron energy distribution seen in Fig. 11. But the number of spikes increases as more material enters the pulse and eventually fill in and smooth out the distribution. In addition, the beam will not remain cold after penetrating the magnetic pulse but will be thermalized under the influence of the increasingly fractionated and randomized magnetic field. Finally, the electron spikes represent population inversions in the energy spectrum and one might expect them to act as sources of free energy for plasma instabilities, e.g. maser-like instabilities. But highly relativistic systems tend to stabilize as most particles have $v \sim c$. Only after the pulse slows via interaction with surrounding material,

would such instabilities become important. These time-scales are beyond those of our simulations and so the asymptotic external particle synchrotron photon spectrum cannot be predicted from our simulation results.

The presence of this external radiation component is a direct result of the pulse interaction with the ambient medium. Due to the low density, the time needed to accumulate enough material to produce observable radiation implies that a delayed emission component arises with respect to the prompt emission from the internal particles.

We conclude this section by summarizing the important limitations of our radiation calculations. We have used the particle distribution function from the simulations that we then use a posteriori to calculate the emission spectra. The particle distribution function can be directly inferred from the PIC calculations because, as stated earlier, the charge to mass ratio of superparticles and particles are the same. Although our calculated spectral break should survive, the actual normalization of the radiation flux cannot be accurately determined because the number of photons does depend on the actual particle number. Another key issue is that radiation reaction terms are not included in our present work. A complete treatment of particle acceleration and radiation should dynamically couple the radiation reaction to the particles and fields each time step. This is beyond the scope of the present work and has been addressed by Noguchi et al. (2005). The effect seems to be to lower the total energy in the radiation. However, all existing simulations presently do not last long enough to know exactly how these results extend to the much longer time scales needed for direct application to astrophysical sources. That remains for future work.

6. The pulses as electron filters

As discussed above, if the pulse width exceeds the proton gyro radius, both, protons and electrons are reflected. This is the case of [27]. If the pulse width is smaller than the proton gyro radius, a critical value of the initial internal plasma β_e^{trans} divides the parameter space into two regions: one in which external electrons are trapped by the pulse and one in which the external electrons pass through. The critical value of β_e^{trans} depends on the temperature of the internal plasma but not its density. The simulation parameters are such that the external protons always pass through the pulse unimpeded. That electrons can be trapped but protons are always transmitted, is important in determining the deceleration rate of the pulses. The pulses can act as filters that accumulate the ambient electrons while allowing the ambient protons to pass through. Such filtering pulses would then decelerate more slowly than standard “snow plow” hydrodynamic outflows in astrophysics that accumulate both electrons and protons.

The average magnetic field in the pulse can be described as a luminosity, i.e. $(B^2/2\mu_0)4\pi R^2 c = L$. Balancing the mechanical or electromagnetic outflow luminosity with the inertia of the ambient matter gives

$$\frac{L}{\Gamma_{\text{pulse}}^2} = 4\pi R^2 c \Gamma_{\text{pulse}} n \Gamma_{\text{pulse}} m c^2, \quad (22)$$

where n is the density of the piled-up ambient medium in the lab frame, m is the constituent particle mass, Γ_{pulse} is the flow Lorentz factor of the pulse and R is the

distance from the source. This yields

$$R = \frac{1}{\Gamma_{\text{pulse}}^2} \sqrt{\frac{L_{\text{obs}}}{4\pi m n c^3}}. \quad (23)$$

If m of the piled-up material is reduced by $m_p/m_e \sim 1836$, the distance the pulse of a given Γ_{pulse} propagates into the ambient medium is increased by a factor of ~ 40 .

6.1. Electron filter survives discharge

How long the electron filtering is maintained depends on how long it takes for the electric field induced by the resulting charge separation to be strong enough to capture the protons.

In the pulse frame, the equation of motion for a single proton in the electric field behind the pulse is given by

$$m_p \frac{dv_p \Gamma}{dt} = -eE = -(e^2/2\epsilon_0)(n_e(t - r/v_p)w - n_0 r(t)), \quad (24)$$

for $w \leq r \leq ct$, where w is the width of the electron layer, r is the distance of the test-proton behind the pulse, n_e is the electron density accumulated in the pulse and n_0 is the ambient proton number density. The second term on the right of the expression for E is due to charge screening by the ambient protons having crossed the pulse unperturbed and filling the downstream region uniformly at a number density n_0 . The retarded time appears in the contribution to E from the electrons in the pulse because its accumulation of electrons takes a time r/v_p to propagate to the proton, where r is measured from the pulse. Using the fact that the total excess electron density at the pulse must equal the proton density left behind $n_e(t)w = n_0 v_p t$.

If we define t_0 as the time at which the given proton crosses the pulse, so $t - t_0 = r/v_p$. We now assume that $v_p \sim c$ for the regime of our calculation. Then the appearance of the retarded time above implies that the electro-static field at the position of the proton at time t is determined by the electron charge density $n_e(t_0)$. Equation (24) becomes

$$\frac{d\Gamma}{dt} \simeq -\frac{e^2}{2\epsilon_0 m_p c} n_0 (ct_0 - r(t)). \quad (25)$$

While Γ can change significantly, v_p remains close to c . We therefore invoke $r(t) \simeq v_p(t - t_0)$ and assume a constant $v_p \simeq c$ for the present calculation. Inserting this expression into (25) yields

$$\frac{d\Gamma}{dt} = -\frac{e^2}{2\epsilon_0 m_p} n_0 (2t_0 - t). \quad (26)$$

Integrating this from t_0 to t gives

$$\Gamma(t) = \Gamma(t_0) - \frac{e^2 n_0}{2\epsilon_0 m_p} \left[2t_0(t - t_0) - \frac{1}{2}(t^2 - t_0^2) \right]. \quad (27)$$

We can then solve for the time $t = \tau$ when Γ falls to $\Gamma(t_0)/2$. The physical solution ($\tau > t_0$) is given by

$$\tau(t_0) \simeq 2t_0 + t_0 \left(1 + \frac{\Gamma_0}{t_0^2} \frac{2\epsilon_0 m_p}{e^2 n_0} \right)^{1/2} \geq 3t_0. \quad (28)$$

To use this result in comparing time scales for the evolution of Γ with models without proton leakage, we must transform this time scale back to the lab frame. Since we

consider the time for Γ_{pulse} to fall only by a factor of 2, in the lab frame, $\tau' \geq \Gamma_0\tau/2$ and $t'_0 \leq \Gamma_0 t_0$, so that $\tau' \geq 1.5t'_0$

That $\tau' > 1.5t'_0$ is important. This implies that proton drag does not significantly reduce the time scale for the relativistic electron dominated pulse to slow down compared to the case in which the protons are ignored. Even at the low limit that is given by $\tau' = 1.5t_0$, the drag exerted on the pulse is only produced by a fraction of the protons. In this case the pulse can be considered to propagate with no additional drag during the last 33% of the propagation: only protons that crossed the pulse at times up to $t'_0 = \tau'/1.5$ can influence the pulse.

7. Application to GRB

In the following section we address several aspects of the DRPA in the context of a PFDO model for GRBs.

In order to make observable predictions, we have to extrapolate our simulation results to times beyond the reach of the simulations. Such extensions bear a number of pitfalls but presently offer the only way to connect the early time micro physics with the observations in the absence of long duration simulations.

Equation (8) allows us to use the fit parameters obtained in Sec. 4 (dashed line in Fig. 8) to estimate the time-scale at which the characteristic frequency of the emitted radiation from the internal electrons reaches a typical value for GRB. Using Eq. (8), and assuming that asymptotically $|B_z|/B_0 \approx 0.12$ (Fig. 9a), the estimated time needed to reach a typical photon energy of E_r can be calculated from

$$\Omega_e^* t_r = \frac{|B_0| \gamma_r^2 - C_0}{B_z 2f} \quad , \quad (29)$$

where γ_r is determined by Eq. (10), E_r and B_0 . B_0 here is not the surface magnetic field of the GRB progenitor but rather the magnetic field in the region where the Poynting flux emerges, which can be farther away from the GRB source and can therefore be smaller. For $E_r = 500 \text{ keV} = h\nu_r$ and $B_0 = 4.473 \text{ T}$, $t_r \approx 0.003 \text{ s}$ which is consistent with reaching this energy before observed prompt GRB time scales demand them.

GRB prompt emission seems to exhibit a double power law emission spectra [1] as observed by BATSE [1, 24]. Remarkably, the photon power law indices obtained from our simulations, $\tau \sim 1.05$ at low and $\tau \sim 2.25$ at high energies, are in excellent agreement with those observed [24].

That being said, the actual power-law break energy cannot be determined from our simulations since the actual photon spectra of observed GRBs are at much higher energies than reached during the duration of our simulations. Our maximum simulation time ($\sim 10^{-6}(B_0/1\text{T})^{-1}\text{sec}$) is too small for the electrons to reach the energies at which they would radiate in the gamma-ray range. In order to reach these energies, simulation times $> 10^{-6}\text{s}$ are needed. We are presently restricted to discussions of the shape rather than true fluxes and energies. From the considerations on saturation of the DRPA we know that the energies of the emitted radiation at saturation are of order $\sim 100 \text{ keV}$, consistent to within an order of magnitude with that of the prompt GRB emission.

In addition to the internal accelerated electrons which are responsible for the prompt gamma-ray emission, the external electrons trapped from the ambient medium would radiate in a later phase. To estimate the onset of their observable contribution,

we must estimate the time evolution of their density increase in the surface layer upstream of the pulse. We assume that this layer is thin compared to the pulse travel distance (thin-shell approximation). In a layer of thickness $\delta r \equiv \delta R/R_0 \ll r(t) \equiv R(t)/R_0$, where R_0 is the initial pulse size, the density increase after a time t is then

$$\frac{n_{\text{shell}}(t)}{n_{\text{ext}}^0} = \frac{1}{3} \frac{r(t)^3 - 1}{r(t)^2 \delta r} . \quad (30)$$

This is valid for spherical expansion, but since the actual situation corresponds to a spherical expansion in a beam of very small opening angle, the slab geometry of our simulations offers an acceptable correspondence. Taking $\delta R = 100c/\omega_e$ and extending this to a time of $t = 10$ s yields a density increase by a factor $n_{\text{shell}}/n_{\text{ext}}^0 \approx 1.7 \cdot 10^9$. Assuming an initial external plasma density $n_{\text{ext}}^0 = 1 \cdot 10^6 \text{m}^{-3}$, corresponding to a typical ISM, $n_{\text{shell}} \approx 1.7 \cdot 10^{15} \text{m}^{-3}$ at this time.

The choice of δr corresponds to observations in our simulations. Increasing its value will decrease the density growth, resulting in a further delay of the emission with respect to the prompt GRB emission. Also depending on n_{ext}^0 and the pulse velocity, this radiation could therefore produce a second peak in the prompt emission or coincide with the GRB afterglow [23].

8. Summary

The present work focuses on the propagation of a Poynting flux dominated relativistic plasma outflow (slab) with an ambient medium. We find that the magnetic outflow breaks up into sub-pulses, consistent with that of the DRPA mechanism [10]. We study the interaction of the leading pulse with the ambient medium. The interaction can now be categorized into three regimes: (a) all external particles are reflected (nearly equivalent to “trapped” for relativistic propagation) by the pulse, (b) all external particles are transmitted, and (c) electrons are reflected but not ions.

In all three regimes, the internal particles originating from within the initial expanding plasma (electrons and positrons) are always trapped and accelerated. External leptons are only trapped in regimes (a) and (c). Regime (a), which is realized when the pulse width is much larger than the proton gyro-radius, is equivalent to the case discussed in the literature by [27]. In contrast, the focus of the present work is on regime (c), which gives rise to a new population of energetic electrons.

For regime (c) the pulse acts as a semi-permeable membrane that filters out electrons from the ambient medium whilst allowing the transmission of ions.

The different behavior of ions and electrons leads to an important difference in the drag force exerted on the pulse by the piled up matter: instead of being immediately felt, the inertia of the protons acts on the pulse with a delay via electrostatic interaction between piled up electrons and transmitted protons. In terms of the propagation time t'_0 of the pulse, only protons that have crossed the pulse at times up to $t'_0 = \tau'/1.5$ can influence the pulse.

In addition to these findings, we have analyzed the particle energy distributions, acceleration rates and synchrotron spectra of the external and internal electrons. We were able to extend the simulation times to $t \approx 160000 \Omega_e^* t$, allowing the study of significantly longer term evolution than in previous work. We find:

- External electrons pile up in a thin shell at the leading flank of the pulse and are accelerated at a rate similar to that of the internal electrons. A fractionally significant amount of radiation (compared to that from internal electrons) from these piled-up

external electrons would occur late stage of the pulse evolution, only when their density has grown large enough.

- The total electron/positron energy quasi-oscillates in exchange with the electromagnetic field energy. However, the Lorentz factor of the pulse continues to grow at the analytically predicted rate throughout the timespan covered by our simulations, as electrons are leaked.
- The internal particles develop a double power-law energy spectrum with a clearly defined break energy. The resulting synchrotron photon spectrum is in remarkable agreement with observations of GRBs [1, 24], though the small time-scales of our simulations prevent us from presently uncovering any additional physics that might modify this spectrum at the later times needed to realistically compare with actual GRB observations, This accelerator will saturate at times of order 0.5 ms due to increasing energy loss via synchrotron emission. The characteristic particle Lorentz factor of a particle whose radiation loss balances its acceleration lies at ~ 100 keV. In the context of GRBs this energy lies within an order of magnitude of the characteristic photon energy of ~ 500 keV.
- While the initial configuration is strongly magnetically dominated, at late times in the simulations, at least 1/2 of the energy is converted into accelerated electrons. While the simulations here represent the physics occurring only at the very front of what would be a much larger scale extended magnetic tower propagating into an ambient medium, the results show that the conversion at the front of the tower is extremely efficient, even without relativistic shocks.

It is now essential to extend the simulations to later times that allow the analysis and comparison of prompt and delayed emission in the course of the DRPA. The goal is to directly connect the initial expansion with the emission of prompt radiation at later times. Our present extrapolations can then be tested. One way to reduce the computational effort is to use a moving window that allows to follow the pulse and simulate only its closer environment. This approach is currently being implemented.

Acknowledgments

We thank A. Frank for use of the ORDA linux cluster and acknowledge support from NSF grant AST-0406799. GP acknowledges support from the Swiss National Science Foundation. EGB acknowledges additional support from the Isaac Newton Institute for Mathematical Sciences, Cambridge UK, and the KITP of UCSB, where this research was supported in part by NSF Grant PHY-9907949.

References

- [1] Band, D., Matteson, J., Ford, L., Schaefer, B., et al., 1993, ApJ, 413, 281
- [2] Birdsall, C.K., Langdon, A.B., 1991, Plasma Physics via Computer Simulation, IOP, Bristol, United Kingdom
- [3] Blackman, E. G., Yi, I., & Field, G. B. 1996, ApJL, 473, L79
- [4] Blandford, R.D., McKnee, C.F., 1976, Phys. Fluids, 19, 1130
- [5] Drenkhahn, G., 2002, A&A, 387, 714
- [6] Katz, J.I., 1997, ApJ, 490, 633
- [7] Kobayashi, S., Piran, T., Sari, R., ApJ, 513, 669–678
- [8] Noguchi, K., Liang, E., and Nishimura, K., 2005, submitted to Physics of Plasmas, preprint (astro-ph/0412310)
- [9] Liang, E., Nishimura, K., 2004, Phys. Rev. Lett., 92/17. 175005-1
- [10] Liang, E., Nishimura, K., Li, H., Gary, S.P., 2003, Phys. Rev. Lett., 90/8, 085001

- [11] Longair, M.S., 1994, *High Energy Astrophysics*, Volume 2, Cambridge University Press (2nd Edition)
- [12] Lyutikov, M. & Blackman, E. G. 2001, *MNRAS*, 321, 177
- [13] Lyutikov, M. & Blandford, R., 2003, preprint (astro-ph/0312347)
- [14] Lyutikov, M., Uzdensky, D., 2003, *ApJ*, 589, 893
- [15] MacFadyen, A. I., Woosley, S. E., & Heger, A., 2001, *ApJ*, 550, 410
- [16] Medvedev, M.V., 2000, *ApJ*, 540, 704
- [17] Medvedev, M.V., Loeb, A., 1999, , *ApJ*, 526, 697
- [18] Mészáros, P., Rees, M.J., 1997, *ApJ*, 482, L29
- [19] Narayan, R., Paczynski, B., Piran, T., 1992, *ApJL*, 395, L83
- [20] Nieter, C., Cary, J.R., 2004, *J. Comput. Phys.*, 196/2, 448
- [21] Nishimura, K., Liang, E., 2003, preprint (astro-ph/0308153)
- [22] Nishimura, K., Liang, E., and Gary, S. P., 2003, preprint (astro-ph/0307456)
- [23] Piran, T., 1999, *Physics Reports*, 314, 575
- [24] Preece, R.D., Briggs, M.S., Mallozzi, R.S., Pendleton, G.N., et al., 2000, *ApJS*, 126, 19
- [25] Rybicki, G.B., Lightman, A.P., 1979, *'Radiative Processes in Astrophysics'*, Wiley, New York
- [26] Sari, R., Piran, T., *ApJ*, 1995, 455, L143
- [27] Smolsky, M.V., Usov, V.V., 1996, *ApJ*, 461, 858
- [28] Spruit, H.C., 1999, *A&A*, 341, L1
- [29] Spruit, H.C., Daigne, F., Drenkhahn, G., 2001, *A&A*, 369, 694
- [30] Thompson, C., 1994, *MNRAS*, 270, 480
- [31] Usov, V.V., 1992, *Nature*, 357, 472
- [32] Weibel, E.S., 1959, *Phys. Rev. Lett.*, 2, 83
- [33] Wheeler, J. C., Meier, D. L., & Wilson, J. R. 2002, *ApJ*, 568, 807